

Non-linear control of high frequency phonons in spider silk

Dirk Schneider¹, Nikolaos Gomopoulos¹, Cheong Y. Koh², Periklis Papadopoulos^{1,3}, Friedrich Kremer⁴, Edwin L. Thomas⁵, George Fytas*^{1,6}

1 Max Planck Institute for Polymer Research, Ackermannweg 10, 55128 Mainz, Germany.

2 Functional and Smart Materials Laboratory, Emerging Systems, DSO National Laboratories, S117605, Singapore.

3 Department of Physics, University of Ioannina, 45110 Ioannina, Greece.

4 Institute of Experimental Physics I, Linnéstr. 5, University of Leipzig, 04103 Leipzig, Germany.

5 Department of Materials Science and Nano-Engineering, Rice University, Houston, Texas 77030 USA.

6 Department of Materials Science University of Crete and IESL-F.O.R.T.H, 77110 Heraklion, Greece

* fyta@mpip-mainz.mpg.de

Spider dragline silk possesses superior mechanical properties^{1,2} compared to synthetic polymers with similar chemical structure due to its hierarchical structure comprised of partially crystalline oriented nanofibrils.^{3,4} To date, silk's dynamic mechanical properties have been largely unexplored. Here we report an indirect hypersonic phononic band gap and an anomalous dispersion of the acoustic-like branch from inelastic (Brillouin) light scattering experiments under varying applied elastic strains. We show the mechanical nonlinearity of the silk structure generates a unique region of negative group velocity, that together with the global (mechanical) anisotropy provides novel symmetry conditions for gap formation.⁵⁻⁸ The phononic band gap and dispersion show strong non-linear strain-dependent behavior. Exploiting material nonlinearity along with tailored structural anisotropy can be a new design paradigm to access new types of dynamic behavior.

Spider dragline silk is commonly regarded as a semi-crystalline biopolymer. Yet despite intensive experimental efforts, the full elucidation of its structural organization and how this relates to its extraordinary macroscopic properties remains elusive¹. The current picture for the dragline fiber structure including the moderately oriented non-crystalline matrix and the more oriented crystals within the nanofibrils is illustrated in Fig. 1d-f.^{2,9-11}. This multilevel structural organization of spider dragline silk leads to its unusual mechanical properties³ including high tensile strength and toughness^{4,12}. A key factor controlling these properties is the pre-strain of the non-crystalline chains, which is created during spinning, and can be relieved when silk is exposed to humidity and allowed to shrink¹³. This “super-contraction” (up to 40%) leads to decreased Young's modulus and increased extensibility¹⁴⁻¹⁶ from the now supercontracted initial length to approximately the maximum strain of the native fiber, imparting upon the spider silk significant

elastic nonlinearity (Fig. 3c,d). While extensive work regarding its quasi-static mechanical properties has been conducted^{12,17}, high frequency mechanical behavior in spider silk remains largely unexplored¹⁸; given the hierarchical structure of spider silk, we expect non-trivial mechanical behavior at hypersonic frequencies. In this work, we employ Brillouin light scattering (BLS) to interrogate the mechanical properties and further elucidate the silk fiber microstructure.

Fibers silked from a *Nephila edulis* spider (Fig. 1a), were wound on the BLS holder creating a grid of parallel fibers (Fig. 1b). Two special scattering geometries were adopted to select the direction of the scattering \mathbf{q} either parallel (q_{\parallel} in Fig. 1g) or normal (q_{\perp} in Fig. 1h) to the fibers [S1].

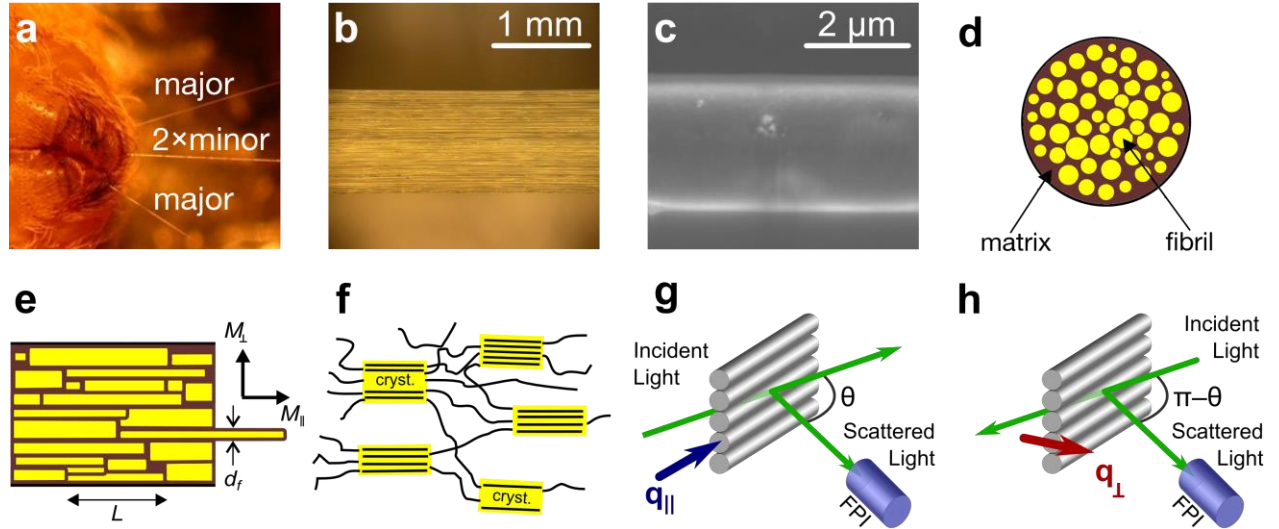


Figure 1| Access to the mechanical properties along and normal to the spider dragline fiber: **a)** Optical microscopy of the spider spinnerets. Both major and minor ampullate fibers are shown, but only the major is used for the BLS experiment. **b)** Grid of parallel major ampullate fibers on the cell holder. **c)** Scanning electron microscope image of a single 2 μm diameter spider dragline silk fiber. **d, e)** Schematic of a single fiber in cross-section and in longitudinal section with mechanical anisotropy (M_{\parallel} and M_{\perp}). The yellow regions are semicrystalline nanofibers with axial (L) and radial (d_f) dimensions and the brown regions are the oriented non-crystalline chains. **f)** Alanine rich highly ordered nanocrystals with size ~ 5 nm (yellow blocks) are interlinked by oriented amorphous glycine-rich chains (indicated as extended lines). **g, h)** Light scattering geometries allowing for probing the elastic constants either parallel (blue) q_{\parallel} or normal (red) q_{\perp} to the fiber axis. The two colored arrows indicate the direction of the scattering wave vector \mathbf{q} with magnitudes: $q_{\parallel} = (4\pi/\lambda) \sin(\theta/2)$ and $q_{\perp} = (4\pi n/\lambda) \sin(\theta/2)$ where θ is the scattering angle and λ the wavelength of the incident laser beam.

In order to determine the complete dynamic mechanical behavior, the full dispersion $\omega(q)$ for a particular polarization state must be known¹⁹. Experimental access to the linearly dispersive portion of $\omega(q)$ is a prerequisite to obtain the acoustic sound velocities and elastic moduli. At high frequencies (GHz), where the phonons are of the appropriate length scale ($\lambda < 300$ nm) for strong interaction with the hierarchically structured spider silk new microstructural information may be obtained. Here, we substantiate the dispersion relation to be significantly more detailed and quite distinct from the linear acoustic regime²⁰.

We focus on phonon propagation along the fiber axis, where interesting dispersion behavior is observed. The symmetric (Stokes- and anti-Stokes process) BLS spectrum exhibits a two doublet spectral line shape (upper panel in Fig. 2a) at $q_{\parallel} = 0.0167 \text{ nm}^{-1}$ for predominantly longitudinally or radially polarized modes. The nature of the peaks labeled (**I**) and (**3**) are unraveled in Fig. 2b [S2]. At long phonon wavelengths (low q_{\parallel} 's in Fig. 2b), mode (**I**) is acoustic with an effective medium sound velocity $c_{\parallel} = \omega/q_{\parallel} = 4970 \pm 30 \text{ m/s}$, i.e. $\sim 60\%$ higher than the speed normal to the fiber axis ($c_{\perp} = 3140 \pm 40 \text{ m/s}$ [S1c]). This value corresponds to a high axial longitudinal modulus, $M_{\parallel} = \rho c_{\parallel}^2 = 31.0 \pm 0.1 \text{ GPa}$ (using bulk density, $\rho = 1.25 \text{ cm}^{-3}$ [S2]) with a lower transversal longitudinal modulus $M_{\perp} = \rho c_{\perp}^2 = 12.3 \pm 0.2 \text{ GPa}$. The large mechanical anisotropy $M_{\parallel} / M_{\perp} = 2.6 \pm 0.05$ (Fig. 3d) of native silk arises from the nanofibrillar structure, consisting of highly oriented “hard” nanofibrils along the fiber axis^{17,21} embedded in a softer non-crystalline matrix (Fig. 1d–f). Importantly, the radially random but axially aligned nanofibril bundles leads to overall structural uniaxial anisotropy causing the large mechanical anisotropy parallel and normal to the silk fiber axis. This has significant consequences to the axial dispersion relation of the fiber at hypersonic length scales.

Experimentally, we observed that the axial dispersion relation (Fig. 2b) shows an unexpected a

large indirect polarization phononic gap at a frequency $f_g \approx 14.8$ GHz and a width $\Delta f_g \approx 5.3$ GHz (hatched area in Fig. 2b), i.e. a normalized gap width $\Delta f_g^\circ (= \Delta f_g / f_g) \approx 0.36$. To the best of our knowledge, this is the first report of a hypersonic phononic band gap in a biological material. A second, more intriguing observation is the anomalous axial ($q_{||}$) dispersion exhibited by band (**I**), which has a region of negative dispersion ($q > q_{||}^* = 0.017 \text{ nm}^{-1}$). Our examination of regenerated silk [S3], i.e., a material without supramolecular structure or overall structural orientation yielded no similar dispersive behavior. The BLS spectra of a regenerated silk film exhibited single doublets for both in-plane and out-of-plane directions (Fig. 2c), corresponding to an isotropic acoustic behavior (Fig. 2d, solid line).

Unlike colloidal crystals⁵ and hybrid superlattices⁶ with a periodic structure at length scales comparable with $\lambda = 2\pi/q_{||}$, the formation of the axial band gap in a silk fiber is not attributable to interference-based Bragg-type scattering⁵ nor particle-resonance induced hybridization^{7,8}. Instead, this is attributed to the cooperative effects between the structural anisotropy and nonlinear elasticity arising from the supramolecular structure of spider silk. Specifically, we show that the anomalous behavior stems from both nanostructured fibrils embedded within an amorphous matrix (forming the ubiquitous signature of an upper cutoff band (**3**) and the mechanical nonlinearity of spider silk, which leads to the anomalous dispersion of the lower band (**I**).

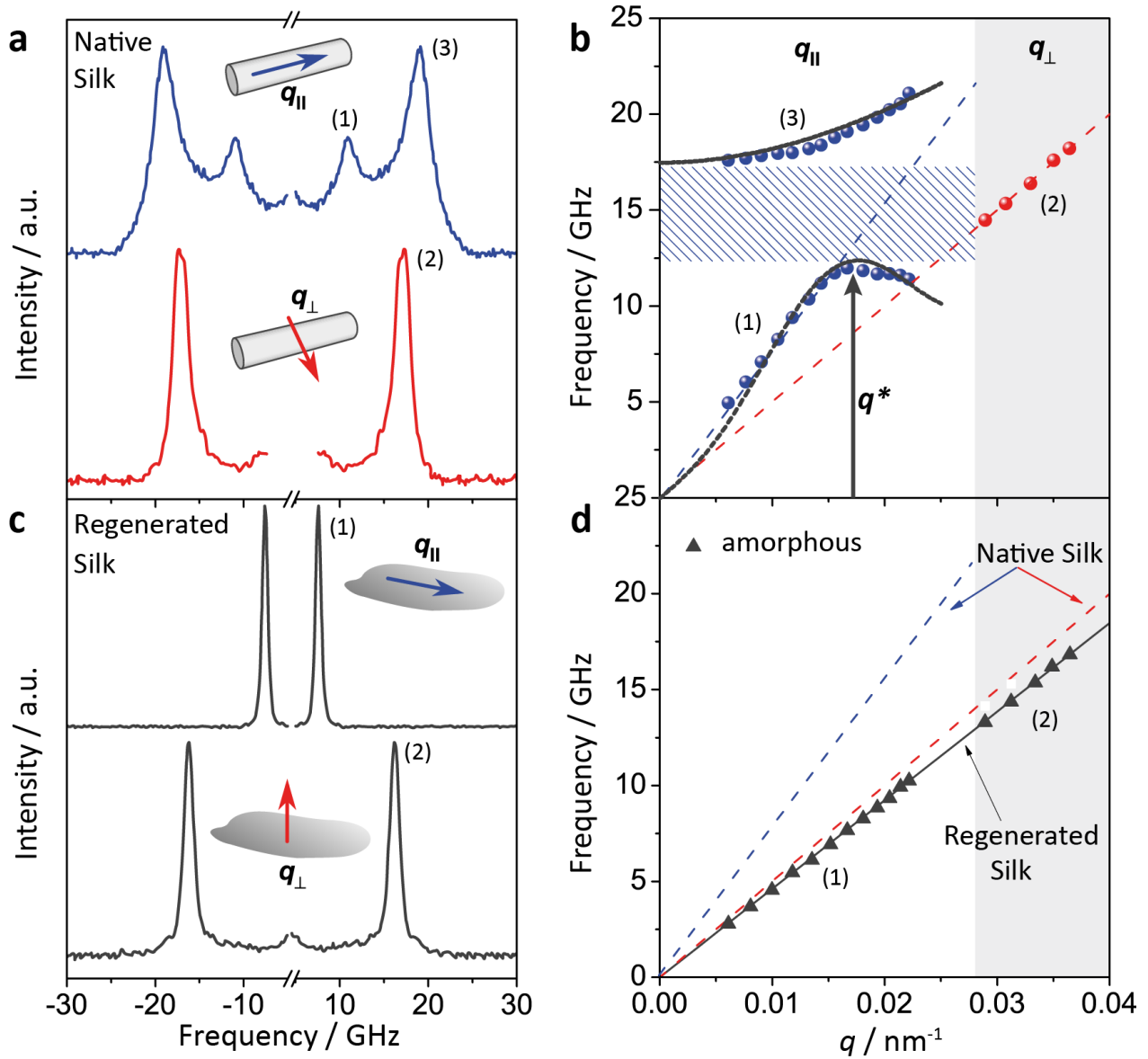


Figure 2| BLS spectra and dispersion diagrams of the native spider dragline silk and regenerated silk. **a)** BLS spectra at $q_{\parallel} = 0.0167 \text{ nm}^{-1}$ (blue) with two peaks (1, 3) along the fiber and at $q_{\perp} = 0.0365 \text{ nm}^{-1}$ (red) with one peak (2) normal to the fiber axis. **b)** Dispersion relations for the three modes representing elastic wave propagation parallel (blue) and normal (red) to the fiber. Straight dashed lines indicate the effective medium sound velocities in the two directions whereas the hatched area denotes the unidirectional stop band. The solid grey lines indicate the dispersion plots obtained from the analytical model. The vertical arrow indicates the crossover q_{\parallel}^* to a negative dispersion region. **c)** Erasure of the gap and mechanical anisotropy in regenerated amorphous and semicrystalline silk: BLS spectra at $q_{\parallel} = 0.0167 \text{ nm}^{-1}$ and $q_{\perp} = 0.0365 \text{ nm}^{-1}$ respectively parallel and normal to the amorphous film. **d)** Linear dispersion relation for the acoustic modes (1) and (2) in the two directions for the amorphous (triangles) regenerated film. The off-axis sound velocity (2) in the native fiber (dashed line) is moderately higher than the sound velocity of the single acoustic phonon in both the regenerated amorphous films.

To substantiate this, we first address the dispersion of band (3). The embedded nanofibrils^{2,9} act as mechanical waveguides, with the eigenmodes classified by their displacement field pattern symmetries²² [S5]. Additionally, there is the signature of cutoff modes (Fig. 2b and Fig. 3a,b at $q_{\parallel} \rightarrow 0$). The degree of positive curvature in the dispersion band (3) is determined by the impedance contrast between the axial shear modulus of the nanofibrils and the surrounding matrix [S5]. The cutoff frequency ($\Omega \sim 17.5$ GHz at $q_{\parallel} = 0$, Fig. 2b) of band (3) is linked intimately to the average lateral dimension of the fibril waveguide and may be estimated by considering a simplified but nevertheless physically representative model [S5], which yields,

$$\Omega \sim \left(\frac{2\mu}{\rho(\Lambda_f - d_f)d_f} \right)^{1/2} \quad (1)$$

where Λ_f , μ and d_f denote respectively, the average lateral separation between nanofibrils ($\Lambda_f \sim 200$ nm), shear modulus of the matrix ($\mu \sim 2\text{--}4$ GPa)²³ and the nanofibril diameter [S5]. This model well represents (Fig. 2b, grey solid line) the experimental dispersion curves (Fig. 2b, Figs. 3a,b) using two adjustable parameters (Λ_f , μ). Considering the uncertainty in nanofibril fraction and shear modulus, d_f falls in the range of 100–140 nm. The successful representation of the cutoff dispersion corroborates existing^{14,16,20} indirect evidence of the nanofibril morphology and dimensions. Importantly, there is no need for specific periodic ordering of the nanofibrils, only the presence of the impedance contrast and the intrinsic uniaxial anisotropy of the nanofibrils are necessary and sufficient for the formation of these cutoff modes [S5].

The anomalous dispersion of mode (I) needs to be understood, in particular in the formation of a negatively dispersive region, including q^* and beyond where the bending of branch (I) occurs [S6]. We propose that this originates from the nonlinearity and nonlocality in the mechanical response, afforded by the micro-structured spider silk [S6c]. The nonlinear stiffening with applied strain leads to improved toughness and strength, has been suggested both theoretically²⁴ and

experimentally²⁵ [S6d]. We further investigated the dynamic behavior of fibers under both increased (stretching) and decreased (supercontraction) pre-strain (Figs. 3a,b). Upon supercontraction, the effective medium sound velocity $c_{\parallel} = 4270 \pm 20 \text{ ms}^{-1}$ decreases by about 15%, (due to decrease of the matrix sound velocity), whereas the bandwidth $\Delta f_{\text{g}}^{\circ} (\approx 0.47)$ increases by 31% (Fig. 3a) [S6]. In comparison, the relaxed amorphous chains (Fig. 1f) stiffen only when significantly stretched ($> 15\%$) [S6b]; similarly, the stress-strain curves of super-contracted silk exhibited a large stress plateau²³. A stronger dependence on strain is anticipated for the native fiber (Fig. 3b), as pre-strained (by spinning) chains strain-stiffen with only a small additional strain. Hence, we observe that at 18% applied strain (Fig. 3b), the speed of sound $c_{\parallel} (= 6260 \pm 60 \text{ ms}^{-1})$ increases by about 27%, whereas $\Delta f_{\text{g}}^{\circ} (\approx 0.24)$ decreases by about 33%, compared to the native fiber. The nonlinear regime is identified by the distinct strain dependence of the longitudinal moduli M_{\parallel} and M_{\perp} (Fig. 3c). While the nonlinearity in the radial direction is weak ($M_{\perp} \sim \text{constant}$), the mechanical anisotropy ($M_{\parallel} / M_{\perp}$) increases significantly with strain (Fig. 3d), corroborating the anticipated strain-induced axial stiffening. Just before failure ($\sim 18\%$ applied strain) the silk fiber reaches an anisotropy of $M_{\parallel} / M_{\perp} \sim 5$ at these high frequencies, notably much higher than in synthetic semi-crystalline systems of similar chemical compositions but unoriented microstructure (Fig. S4).

The observed decrease of q^* (bending of the lower branch) at 18% strain clearly reflects the increase in the velocity of mode (I), consistent with strain-induced stiffening (Fig. 3b). To account for the trend with varying strain (Fig. 3a, b), from high extension (+18%) to supercontraction (-20%), we consider the nonlocal elastic nonlinearity in the spider silk utilizing a discretized lattice model to capture the nonlocality imparted by the pre-strain distributions in the amorphous matrix (Fig. 3e). The nonlinearity is included through anharmonicity up to the fourth order^{26,27} [S6c]. In the dispersion relation,

$$\omega(k, u_0) = \frac{2c_{linear}}{a_0} \sin\left(\frac{qa_0}{2}\right) F_{nonlinearity}(q), \quad (2)$$

where u_0 is the pre-strain, a_0 is the discretization length-scale that captures the “effective” structural nonlocality in the medium arising from the pre-strain distribution in the amorphous matrix [S6c], and $F_{nonlinearity}(q)$ accounts for the nonlinearity through higher order stiffness constants [S6]. This simplified model captures the dynamics because the displacement fields are predominantly polarized in the axial direction, i.e. we are examining eigenmodes of the same pseudo “one-dimensional” structure. The 1D analytical solutions show good agreement with the experimental dispersion relations in Figs. 3a and 3b. Several defining features of the nonlinear mechanical responses (Fig. 3a,b) are well modeled, particularly the dispersion band (**I**), which is commonly associated with the “acoustic” branch. For the native fiber, the maximum strained fiber and the super-contracted fiber, the vanishing group velocity at q^* is followed by a dispersion with negative curvature (Figs. 2b,3a,3b), a clear signature of nonlocality (Fig. 3e) [S6c,d]. This unique nonlocal, nonlinearity imbues spider silk with a region of negative group velocity enabling negative refraction and potential focusing of hypersonic phonons.

The cutoff frequency of band (**3**) remains unchanged under supercontraction (at -20%), although the effective medium sound velocity decreases (Fig. 3a). In contrast to an anticipated band bending at a larger q^* as expected from hybridization, it occurs at the same q^* , albeit now at a lower frequency (10.7 GHz instead of 12.2 GHz); this decrease is predominantly due to reduced nonlinearity [S6c], consistent with supercontraction. Under large strains ($\sim 20\%$), a lowered cutoff frequency Ω and a higher effective medium sound velocity are observed (Fig. 3b).

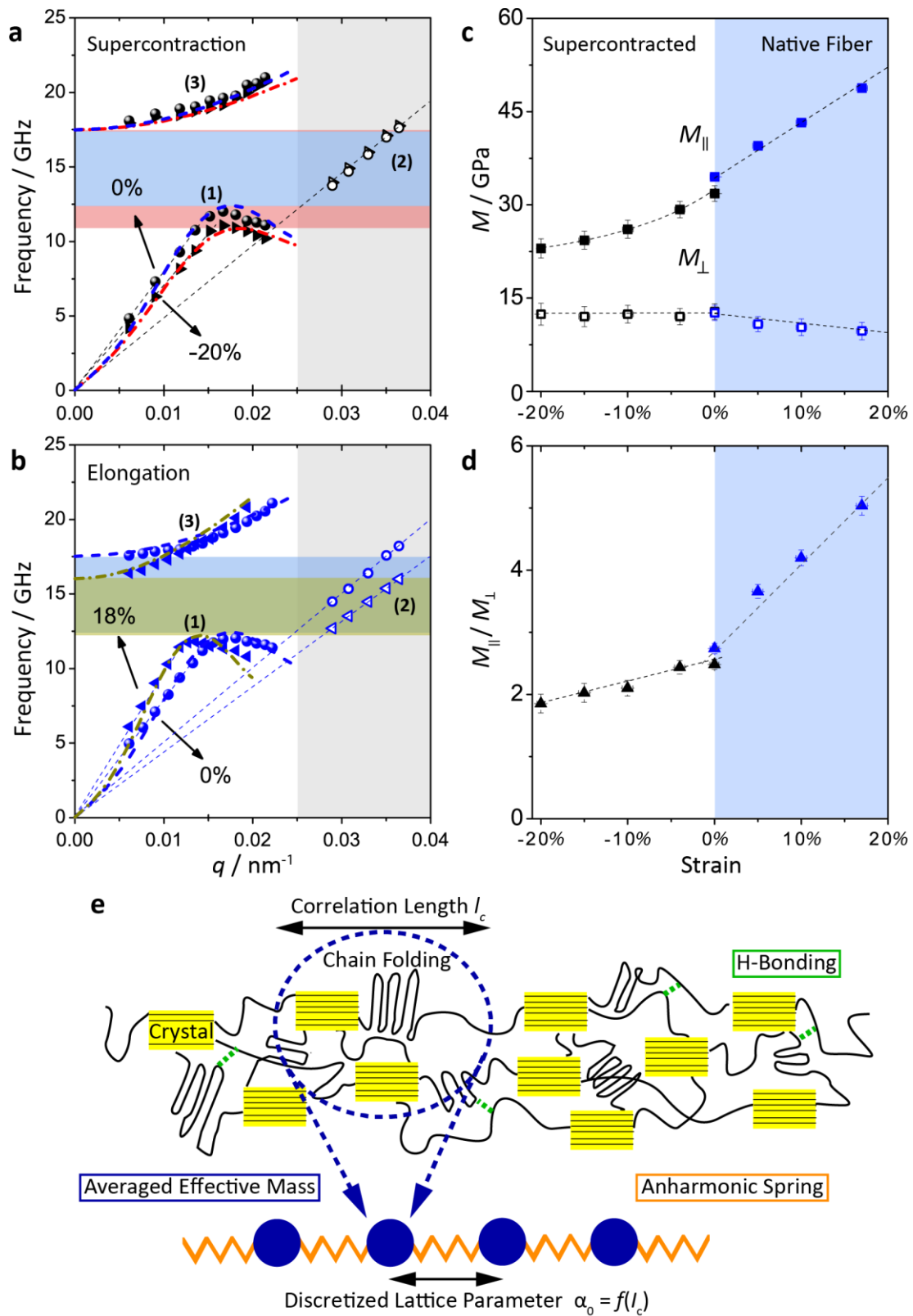


Figure 3| The effect of strain on the dispersion diagram and the mechanical anisotropy of native and supercontracted fibers. Dispersion diagrams for wave propagation parallel (modes (1), (3)) and normal

(mode (2) (at $q_{\perp} \geq 0.025 \text{ nm}^{-1}$ in the shaded area) in **a**) supercontracted fibers at -20% (\blacktriangleright , \triangleright), overlay with the analytical dispersion plot (red dashed-dot) and 0% strain (\bullet , \circ), overlay with the analytical dispersion plot (blue dashed) and **b**) in native fibers at 0% (\bullet , \circ) and 18% applied strain (\blacktriangleleft , \triangleleft), overlay with the analytical dispersion plot (olive dashed-dot). Strain values are calculated with respect to the unstretched native fiber length and hence the values for the supercontracted sample are negative. The hatched areas denote the unidirectional stop band in a supercontracted (**a**) and stretched fiber compared to the native fiber in **b**). **c**) Longitudinal moduli parallel and normal to the fiber for the native (\blacksquare , \square) and supercontracted (\blacksquare , \square) silk. **d**) Mechanical anisotropy vs. strain for the native (\blacktriangle) and supercontracted (\blacktriangle) silk. Error bars show the uncertainty of modulus due to the error in measuring fiber diameter. **e**) Top. Schematic of the microstructure of the spider silk fiber consisting of nanocrystals interlinked by a fraction of pre-stretched chains in the amorphous matrix. This presents spatial stress and strain gradients, which translates into a non-local correlation length l_c that imparts the spatial dispersivity similar to a lattice. Bottom. Schematic of the equivalent anharmonic linear chain, with the discretized lattice parameter α_0 utilized to capture this non-locality in the amorphous matrix.

In contrast to hybridization^{7,8,28}, the band bending is instead laterally shifted to lower q^* values and occurs at approximately the same frequency due to increased nonlinearity and nonlocality as the amorphous chains stretch and become more aligned, both effects physically consistent with strain-induced stiffening. The analytical dispersion plots (Fig. 3a,b) further suggest that nonlinearity also contributes to the linear acoustic velocity increase at low q values [S6d]. Based on the corroboration between our analytical model [S6c,d] and the experimentally observed trends at various strains employing minimal number (all physical) fitting parameters, the behavior of the acoustic band (I) is certainly a result of nonlinear elasticity with applied strain.

In summary, the observation of a hypersonic phononic band gap and presence of a negatively dispersive region in a natural material are reported. Through a nonlinear 1D lattice chain model, these features are attributed to the intriguing and subtle interplay between the (i) uniaxial symmetry of the nanofibrils and (ii) nonlocal nonlinear mechanical behavior of the surrounding inhomogeneous amorphous polymer matrix. The interrogation of the silk by phonon propagation at short length scales reveals the major role played by the multilevel structural organization and the influence of nonlinearity on axial elastic energy flow in spider silk, distinctly with a wide low

frequency band gap, in the absence of any discrete structural periodicity or resonance based hybridization^{7,8}. This finding provides an intriguing principle towards novel routes to tunable dynamic metamaterials by meshing symmetry with material nonlinearity, and generalizing discrete periodicity with spatial non-locality. Similar findings are anticipated in a manifold of active natural²⁹ and hybrid hierarchical materials³⁰, pointing towards rich possibilities from bio-inspiration for the rational design of dynamic materials.

References

SI Reference to section in the supplementary information are indicated in square bracket

1. Giesa, T., Arslan, M., Pugno, N. M. & Buehler, M. J. Nanoconfinement of Spider Silk Fibrils Begets Superior Strength, Extensibility, and Toughness. *Nano Lett.* **11**, 5038–5046 (2011).
2. Sapede, D. *et al.* Nanofibrillar Structure and Molecular Mobility in Spider Dragline Silk. *Macromolecules* **38**, 8447–8453 (2005).
3. Vollrath, F., Madsen, B. & Shao, Z. The effect of spinning conditions on the mechanics of a spider's dragline silk. *Proc. R. Soc. B Biol. Sci.* **268**, 2339–2346 (2001).
4. Agnarsson, I., Kuntner, M. & Blackledge, T. A. Bioprospecting Finds the Toughest Biological Material: Extraordinary Silk from a Giant Riverine Orb Spider. *PLoS ONE* **5**, e11234 (2010).
5. Cheng, W., Wang, J., Jonas, U., Fytas, G. & Stefanou, N. Observation and tuning of hypersonic bandgaps in colloidal crystals. *Nat. Mater.* **5**, 830–836 (2006).
6. Schneider, D. *et al.* Defect-Controlled Hypersound Propagation in Hybrid Superlattices. *Phys. Rev. Lett.* **111**, 164301 (2013).
7. Still, T. *et al.* Simultaneous Occurrence of Structure-Directed and Particle-Resonance-Induced Phononic Gaps in Colloidal Films. *Phys. Rev. Lett.* **100**, 194301 (2008).
8. Lemoult, F., Kaina, N., Fink, M. & Lerosey, G. Wave propagation control at the deep subwavelength scale in metamaterials. *Nat. Phys.* **9**, 55–60 (2013).
9. Miller, L. D., Putthanarat, S., Eby, R. & Adams, W. . Investigation of the nanofibrillar morphology in silk fibers by small angle X-ray scattering and atomic force microscopy. *Int. J. Biol. Macromol.* **24**, 159–165 (1999).
10. Poza, P., Pérez-Rigueiro, J., Elices, M. & LLorca, J. Fractographic analysis of silkworm and spider silk. *Eng. Fract. Mech.* **69**, 1035–1048 (2002).
11. Gould, S. A. C., Tran, K. T., Spagna, J. C., Moore, A. M. F. & Shulman, J. B. Short and long range order of the morphology of silk from *Latrodectus hesperus* (Black Widow) as characterized by atomic force microscopy. *Int. J. Biol. Macromol.* **24**, 151–157 (1999).
12. Yang, Y. *et al.* Toughness of Spider Silk at High and Low Temperatures. *Adv. Mater.* **17**, 84–88 (2005).
13. Savage, K. N., Guerette, P. A. & Gosline, J. M. Supercontraction Stress in Spider Webs. *Biomacromolecules* **5**, 675–679 (2004).

14. Guinea, G. V., Elices, M., Pérez-Rigueiro, J. & Plaza, G. R. Stretching of supercontracted fibers: a link between spinning and the variability of spider silk. *J. Exp. Biol.* **208**, 25–30 (2005).
15. Ene, R., Papadopoulos, P. & Kremer, F. Supercontraction In Nephila Spider Dragline Silk - Relaxation Into Equilibrium State. *Polymer* **52**, 6056–6060 (2011).
16. Ebenstein, D. M. & Wahl, K. J. Anisotropic nanomechanical properties of Nephila clavipes dragline silk. *J. Mater. Res.* **21**, 2035–2044 (2011).
17. Glišović, A., Vehoff, T., Davies, R. J. & Salditt, T. Strain Dependent Structural Changes of Spider Dragline Silk. *Macromolecules* **41**, 390–398 (2008).
18. Mortimer, B. *et al.* The Speed of Sound in Silk: Linking Material Performance to Biological Function. *Adv. Mater.* **26**, 5179–5183 (2014).
19. Cusack, S. Variation of Longitudinal Acoustic Velocity at Gigahertz Frequencies with Water Content in Rat-Tail Tendon Fibers. *Biopolymers* **23**, 337–351 (1984).
20. Koski, K. J., Akhenblit, P., McKiernan, K. & Yarger, J. L. Non-invasive determination of the complete elastic moduli of spider silks. *Nat. Mater.* **12**, 262–267 (2013).
21. Lefèvre, T., Boudreault, S., Cloutier, C. & Pérolet, M. Conformational and Orientational Transformation of Silk Proteins in the Major Ampullate Gland of Nephila clavipes Spiders. *Biomacromolecules* **9**, 2399–2407 (2008).
22. Davydov, S. L., Zaretskii-Feoktistov, G. G. & Sudakov, V. V. Propagation of axially symmetric elastic vibrations along a waveguide in an elastic medium. *Polym. Mech.* **10**, 90–94 (1974).
23. Pérez-Rigueiro, J., Elices, M. & Guinea, G. V. Controlled supercontraction tailors the tensile behaviour of spider silk. *Polymer* **44**, 3733–3736 (2003).
24. Keten, S., Xu, Z., Ihle, B. & Buehler, M. J. Nanoconfinement controls stiffness, strength and mechanical toughness of β -sheet crystals in silk. *Nat. Mater.* **9**, 359–367 (2010).
25. Cranford, S. W., Tarakanova, A., Pugno, N. M. & Buehler, M. J. Nonlinear material behaviour of spider silk yields robust webs. *Nature* **482**, 72–76 (2012).
26. Parnes, R. Dispersion relations of waves in a rod embedded in an elastic medium. *J. Sound Vib.* **76**, 65–75 (1981).
27. Askar, A. Dispersion Relation and Wave Solution for Anharmonic Lattices and Korteweg De Vries Continua. *Proc. R. Soc. Lond. Math. Phys. Sci.* **334**, 83–94 (1973).
28. Alonso-Redondo, E. *et al.* A new class of tunable hypersonic phononic crystals based on polymer-tethered colloids. *Nat. Commun.* **6**, 8309 (2015).
29. Teyssier, J., Saenko, S. V., van der Marel, D. & Milinkovitch, M. C. Photonic crystals cause active colour change in chameleons. *Nat. Commun.* **6**, 6368 (2015).
30. Lee, S.-M. *et al.* Greatly Increased Toughness of Infiltrated Spider Silk. *Science* **324**, 488–492 (2009).

Acknowledgments: The work was partially supported by Aristeia Program-285 (EU, GSRT-Greece), ERC-AdG-694977, SFB TRR102 and DFG (Grant No. BU 1556/27).

Author Contributions: D. S. and N. G. contributed equally to the BLS measurements. P. P. fabricated the samples. C. Y. K. developed the theoretical description of the dispersion diagrams. G. F. planned the project and wrote most of the article; C. Y. K., P. P., F. K. and E. L. T. corrected

and finalized it. All authors have discussed the results and commented on the manuscript.

Additional Information: Supplementary information is available in the online version of the paper. Correspondence and requests should be addressed to George Fytas.

Competing Financial Interests: The authors declare no competing financial interests.

Methods

Sample preparation Adult *Nephila edulis* spiders, fed on a diet of crickets, were forcibly silked to get major ampullate silk. For this, awake spiders were placed into a bag with needles between their legs and silk was pulled from their glands with sticky tape. We monitored the spiders with a microscope to ensure that we collected silk only from the two major ampullate glands. Silk from other glands, such as minor ampullate, was separated with needles and fixed to the side with sticky tape. A motorized setup wound the major ampullate silk at a fixed speed of 1 cm/s around a holder consisting of four metal rods with a distance of 2 cm between them. This way a 2 mm-wide grid of evenly spaced spider silk fibers was obtained. Silk was further glued with two-component epoxy adhesive onto a metal holder for Brillouin light scattering experiments.

Brillouin light scattering (BLS) BLS utilizes the scattering of a probe laser beam from thermally activated phonons along a specified direction defined by the scattering vector q . The magnitude of the scattering vector, q is independent from the refractive index in transmission geometry (Fig. 1g) $q_{||} = (4\pi/\lambda) \sin(\theta/2)$, where $\lambda = 532$ nm is the laser wavelength in vacuum wavelength and θ is the scattering angle, whereas, in the reflection geometry (Fig. 1h), $q_{\perp}(n)$ depends on the refractive index. The inelastic interaction between the incident photons and thermal phonons is evidenced in the frequency shift $f(q)$ of the BLS spectrum at hypersonic (GHz) frequencies, resolved by a high-resolution tandem Fabry–Perot interferometer (JRS Instruments). Longitudinal (transverse) displacements have associated a VV (VH) polarization, selected by the input polarizer (V) and output analyser (V or H); V(H) denotes vertically (horizontally) polarized light relatively to the scattering (sagittal) plane.

Analytical Calculations To calculate the dispersion relation of mode $\mathfrak{3}$, a single nanofibril, embedded in an amorphous matrix was considered. Due to the random orientation of the nanofibrils radially across the fiber, the nanofibrils were considered to be non-interacting [Ref. S16,S20]. Hence it suffices to consider an isolated nanofibril embedded within a softer, amorphous matrix. Due to the selection rules of the BLS, one

may consider only the longitudinal equation of motion of a stiff rod subjected to shear forces from the softer matrix along its boundaries. The critical requirement for this dispersion is in the presence of shear moduli contrast between the nanofibril and the amorphous matrix and was verified with full 3D numerical calculations across a wide range of moduli for both the nanofibril and the matrix. (see section S5 in the Supplemental information for details).

To calculate the dispersion relation of mode I , the spider silk is considered to possess strain gradients due to prestrain imparted during silk spinning that causes considerable strain inhomogeneity in the semi-oriented amorphous matrix. This spatial non-locality may be in turn represented physically by a discretized lattice chain [Ref. S42-S49], linked to an equivalent non-local correlation length arising from the strain gradients. We checked that this non-local correlation length is consistent with independently obtained (numerically and experimental) values (approximately 20 nm). The elastic nonlinearity within the spider silk, which occurs either during strain softening (supercontraction) or strain hardening (stretching), is represented by an anharmonic potential to the 4th order overlaid onto the same discretized lattice chain to retain the same physical nonlocality. The renormalized Poincare method [Ref. S50], is then adopted to avoid divergent secular terms (see section S6 in the Supplemental information for details) to finally obtain the dispersion relation in eqn (2) (see also S6.4 and S6.5).

3D Simulations All the 3D simulations were performed using the eigensolver of the finite element simulation software Comsol Multiphysics. As the radial arrangements of the nanofibrils were random, all simulations were conducted on both square as well as triangular lattices to identify that the eigenmodes of interest were independent of the specific periodicity and lattice type. The unit cells that were investigated were simulated by applying Bloch periodic boundary conditions to retrieve the radial dispersion relation and to ascertain whether the dispersion relation of the spider silk belonged to the cermet or network topology class [Ref. S7-9] (refer to section S2 in the Supplemental information for details and the parameters utilized in the simulations. The eigenfrequencies at $q_{\parallel}=0$ for both axis-symmetric and non-axis-symmetric cross sections of the nanofibril the calculations revealed robustness to in the shear moduli contrast between the nanofibril and the amorphous matrix satisfying the predominantly axially polarization of this eigenmode (Fig. S5d). Section S5 of the Supplemental information further presents details and discussion on the conditions for the particular eigenmode symmetry in order to preserved the quasi-longitudinal polarization and its insensitivity to variation of specific inter-fibril spacings.